Journal of
*Marine Science
and Engineering*

MDPI

Article

Numerical Evaluation of the Wave-Making Resistance of a Zero-Emission Fast Passenger Ferry Operating in Shallow Water by Using the Double-Body Approach

Suleyman Duman , Evangelos Boulougouris *, Myo Zin Aung , Xue Xu and Amin Nazemian

Department of Naval Architecture, Ocean and Marine Engineering, University of Strathclyde,
Glasgow G4 0LZ, UK
* Correspondence: evangelos.boulougouris@strath.ac.uk

Abstract: The consideration of shallow water effects has gained in importance regarding inland operations. The interaction between the keel and the riverbed affects the hydrodynamic characteristics of marine vessels. The highly complex nature of the interference phenomenon in catamarans makes the shallow water problem more complicated as compared to monohulls. Hence, catamarans are very sensitive to speed changes, as well as to other parameters, such as the shallow water effects. This makes the design of catamarans more challenging than their monohull equivalents. At lower Froude numbers, the higher importance of the frictional resistance makes the greater wetted surface of the catamaran a disadvantage. However, at higher speeds, there is the potential to turn their twin hulls into an advantage. This study aims to investigate the wave-making resistance of a zero-carbon fast passenger ferry operating in shallow water. The URANS (unsteady Reynolds-averaged Navier–Stokes) method was employed for resistance simulations. Then, the double-body approach was followed to decompose the residual resistance into viscous pressure and wave-making resistance with the help of the form factors of the vessel calculated at each speed. The characteristics of the separated wave-making resistance components were obtained, covering low, medium, and high speeds. Significant findings have been reported that contribute to the field by providing insight into the resistance components of a fast catamaran operating in shallow waters.

Keywords: wave-making resistance; shallow water; form factor; double-body; wave interference; catamaran; URANS; CFD

check for updates

Citation: Duman, S.; Boulougouris, E.; Aung, M.Z.; Xu, X.; Nazemian, A. Numerical Evaluation of the Wave-Making Resistance of a Zero-Emission Fast Passenger Ferry Operating in Shallow Water by Using the Double-Body Approach. *J. Mar. Sci. Eng.* **2023**, *11*, 187. https://doi.org/10.3390/jmse11010187

Academic Editors: Carlos Guedes Soares and Serge Sutulo

Received: 23 November 2022
Revised: 14 December 2022
Accepted: 2 January 2023
Published: 11 January 2023

1. Introduction

Fast and green transportation systems are becoming indispensable parts of our lives as they have the potential to provide a sustainable future. Some of them, such as ground vehicles, are already being used by a considerable number of people, and other types of vehicles are in a transition period or under feasibility assessment. Most of the metropolis and shore cities in the world rely on waterborne transportation to carry passengers on a daily basis from one port to the other. Providing large deck areas and having an immense potential to travel at high speeds, with relatively less power compared to equivalent monohull examples, catamarans are strong candidates for marine transportation.

The implementation of high-fidelity solution techniques is relatively new compared to the overall progress on fluid dynamics. RANS solvers emerged in the early 21st century and have become an indispensable part of the design, optimization, and simulation of engineering systems. CFD is now widely used in marine hydrodynamic problems, e.g., power predictions, manoeuvring simulations, and marine propeller design. Molland et al. (1994) investigated the resistance of symmetric catamarans [1]. Insel and Doctors (1995) presented a method to capture the wave patterns of monohulls and catamarans by linearized theory [2]. Van't Veer (1998) conducted experiments to evaluate the resistance and seakeeping performance characteristics of the Delft catamaran 372 (DC372) [3]. Castiglione et al. (2011)

investigated the seakeeping characteristics of DC372 in rough seas with URANS [4]. Milanov (2012) developed a manoeuvring model that is a function of advance speed and water depth for a water-jet-driven fast catamaran [5]. Broglia et al. (2014) investigated the wave interference phenomena between the demihulls of DC372 by conducting experiments at different demihull clearance arrangements [6]. Duman et al. (2020) utilized the double-body approach in CFD simulations to predict the wave interference of a trimaran surface combatant using form factors [7]. Basic et al. (2020) introduced an improved method of the original linear wave-making theory to predict the wave-making resistance of ships [8]. Papanikolaou et al. (2020) presented a study focusing on the hydrodynamic hull form optimization of a zero emission, battery driven, fast catamaran vessel [9]. Boulougouris et al. (2021) presented the implementation of state-of-the-art "Industry 4.0" methods and tools to enable fully electrical, fast, zero-emission waterborne urban transport [10]. Shi et al. (2021) conducted an extensive study to predict the shallow water effects acting on a zero-carbon fast passenger catamaran [11]. Duman and Bal (2022) applied the CFD method to DC372 to develop a non-linear manoeuvring mathematical model that can work at relatively high Froude numbers [12]. Ulgen and Dhanak (2022) analysed the hydrodynamic performance of an unmanned catamaran, WAM-V, in restricted waters by using OpenFOAM® [13].

This study was conducted as part of an ongoing H2020 project TrAM: Transport, Advanced and Modular to evaluate the hydrodynamic performance of the Stavanger Demonstrator of TrAM in shallow water conditions at a relatively low draught loading. The reason for choosing the presented operational conditions is to analyse the vessel's hydrodynamic performance in a different environment; in the present case, to keep the operational conditions as close to the Thames River as possible. First, the Stavanger Demonstrator was subjected to 2-DoF CFD simulations in deep and shallow water conditions to calculate the resistance performance and dynamic attitude. The computational analysis covers a wide range of Froude numbers between 0.20–0.66. Then, the catamaran hull was analysed by utilizing the double-body approach in CFD simulations. Single-phase simulation results have been used to calculate the form factors of the catamaran at all speeds. The residual resistance components that come from the 2-DoF resistance analysis have been decomposed into frictional and wave-making resistance components with the help of those form factors. Significant findings have been reported that contribute to the field of marine hydrodynamics by providing detailed insight into the resistance components of the subject vessel.

2. Mathematical Models

2.1. Geometric Properties of the Catamaran Hull

The catamaran hull form is designed for carrying passengers with fully electric power as part of TrAM, an ongoing EU-funded project [14]. The first demonstrator of the TrAM project, Stavanger Demonstrator, was launched and named MS Medstraum in Stavanger, Norway to provide zero-emission transportation with a maximum of 27 kn recorded speed (Figure 1). With these features, Stavanger Demonstrator is a special design as it is the world's first 100% battery-driven fast passenger ferry.

The catamaran hull form is characterized by a slender body, an axe-shaped bow, a flow-adopted propeller tunnel, a transom stern, and a bow thruster tunnel (Figure 2). The fully-appended Stavanger Demonstrator used in this study includes a twisted rudder, a shaft, and two symmetrical foil-shaped struts on both the port and starboard sides.

The main dimensions of the Stavanger Demonstrator are given in Table 1 in nondimensional form. Two different loading conditions (LC) have been analysed by the CFD method: $T' = 0.045$ (LC1) and $T' = 0.040$ (LC2). The displacement is changed by only re-arranging the draught position without any modification on the original Stavanger Demonstrator hull form to obtain main particulars for the LC2.

Figure 1. The Stavanger Demonstrator of the H2020 TrAM Project: MS Medstraum.

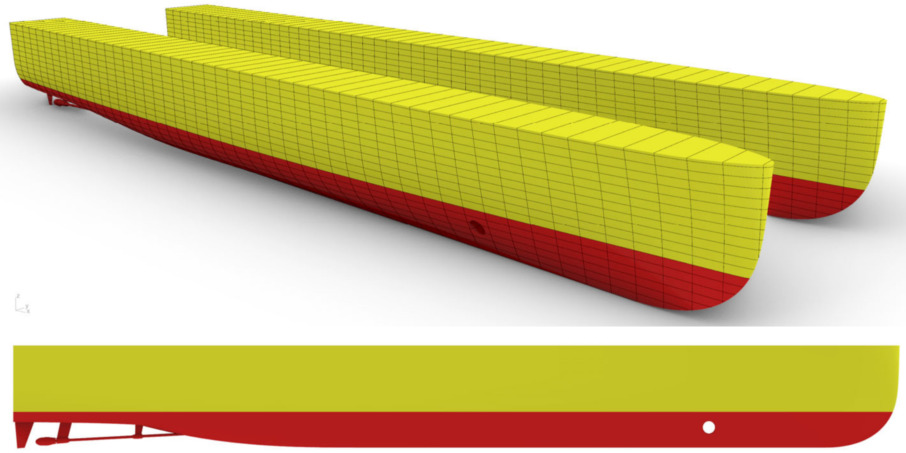

Figure 2. Hull surface in 3-D from the perspective (**upper**) and profile (**lower**) views.

Table 1. Principal dimensions of the Stavanger Demonstrator.

Dimension	Nondim.	Nondim. Value
Separation (s)	s/Lpp	0.227
Draught (T)	T/Lpp	0.040
KB	KB/Lpp	0.026
LCB	LCB/Lpp	0.460

2.2. Computational Method

All the hydrodynamic analyses of the Stavanger Demonstrator reported here have been done at model scale by using the commercial RANS solver software Star-CCM+ [15]. This chapter presents the field equations, boundary conditions, discretization of the computational domain, form factor calculation approach and the nondimensionalisation procedure followed in this study.

2.2.1. Governing Equations

Resistance simulations of the Stavanger Demonstrator are practised under 2-DoF conditions to allow the vessel to move freely on a vertical plane passing by the longitudinal symmetry centre. The flow field is built in two phases (water and air) by defining a free surface interaction level in a vertical direction (z-axis). The initial state of the free water surface is set to a flat plane where the ship floats at a laden draught. The volume of fluid (VoF) method is implemented to control the phase changes between the pre-described water and air cells [16]. As the vessel is released, any kind of motion or disturbance will cause gravity waves that will initiate a sequence of free surface waves in the vicinity of the vessel.

The fluid flow inside the computational domain is assumed to be Newtonian, incompressible, and turbulent. The fluid flow for both phases is handled by the Navier–Stokes equations in 3-dimensional space. Multi-phase flow simulations are achieved by solving the continuity equation (Equation (1)) and the Reynolds-averaged Navier–Stokes (RANS) equations (Equation (2)) in an unsteady way. As a result of averaging operation to the original Navier–Stokes (momentum) equations, Reynolds stresses (Equation (3)) appear that are modelled by the turbulence model. The near-wall treatment is activated within the turbulence model, Realizable k-epsilon, by setting the dimensionless wall distance (y+) to be between 30–300, which enables the wall function near the no-slip walls. Timestep, one of the key parameters for well-posed unsteady solutions, is determined according to the ITTC recommendations [17] following Equation (4) and is kept constant as all the computations are based on the implicit solution algorithm.

$$\frac{\partial(\overline{u}_i)}{\partial x_i} = 0 \tag{1}$$

$$\frac{\partial(\overline{u}_i)}{\partial t} + \overline{u}_j \frac{\partial(\overline{u}_i)}{\partial x_j} + \frac{\partial\left(\overline{u_i' u_j'}\right)}{\partial x_j} = -\frac{1}{\rho}\frac{\partial \overline{p}}{\partial x_j} + \frac{\partial \overline{\tau}_{ij}}{\partial x_j} \tag{2}$$

$$\overline{\tau}_{ij} = \nu\left(\frac{\partial \overline{u}_i}{\partial x_j} + \frac{\partial \overline{u}_j}{\partial x_i}\right) \tag{3}$$

$$\Delta t = 0.005 \ \div 0.01\frac{L}{V} \tag{4}$$

2.2.2. Computational Domain Boundaries and Grid Resolution

The sizes of the computational domain mainly depend on the type of the physical problem. Dimensions should provide adequate clearance for the initialization of the solution and for the developing flow without having an undesired numerical error. When previous CFD studies are searched, it is seen that at least 1.5 L upstream, 3 L downstream, and 2 L clearance are very common and give sufficient enough space to allow free surface waves to be developed for conventional resistance simulations. Bottom and top boundaries are generally assigned 1 L to 1.5 L far from the floating body. By considering previous experiences and recommendations and customize them to Stavanger Demonstrator, 2.37 L and 3.75 L distances are set for the CFD simulations in the upstream and downstream directions, respectively. Since there is no superstructure in the model geometry, the top boundary is located 1.68 L in height from the origin of the coordinate system, which is assigned at the intersection point of the aft perpendicular and keel of the vessel. The side boundaries are located approximately 2.25 L away from the centreline (Table 2). To avoid the bank shallow water effects in deep water simulations, an artificial infinite boundary effect is achieved by setting the top, bottom, and side faces as inlets where the fluid flows in the longitudinal direction, and yet no flux enters the domain from these faces. For the shallow water analysis, on the other hand, the bottom boundary is set to a pre-described depth and assigned as a no-slip moving wall, which has the same velocity as the free stream imposed at the inlet faces. This technique provides an identic solution to the physical operational conditions.

Table 2. Domain dimensions in CFD simulations.

Boundaries	**Background (× L)**	**Overset (× L)**
Upstream	2.370	0.072
Downstream	3.745	0.037
Top	1.685	0.169
Bottom	1.685	0.015
Side	2.247	0.187

The boundary conditions used in the CFD simulations are shown in Figure 3. The computational domain is divided into two main regions: background and overset. In the background domain, the front, top, bottom, and side faces are assigned as velocity inlets; the back face is set to outlet; and the boundary face on the centreline of the catamaran is set to symmetry conditions. In the overset domain: all faces except the boundary face on the centreline, which is set to symmetry, are assigned as overset boundaries. The Stavanger Demonstrator hull is assigned as a no-slip wall, where the tangential and normal velocities are zero on the hull surface. The Chimera or overset facilitates large amplitude motions without any deformation on the grid cells around the moving body. The flow features, such as velocity and pressure, are transferred between the overset boundaries and the background overlapping cells through the intersecting points [18].

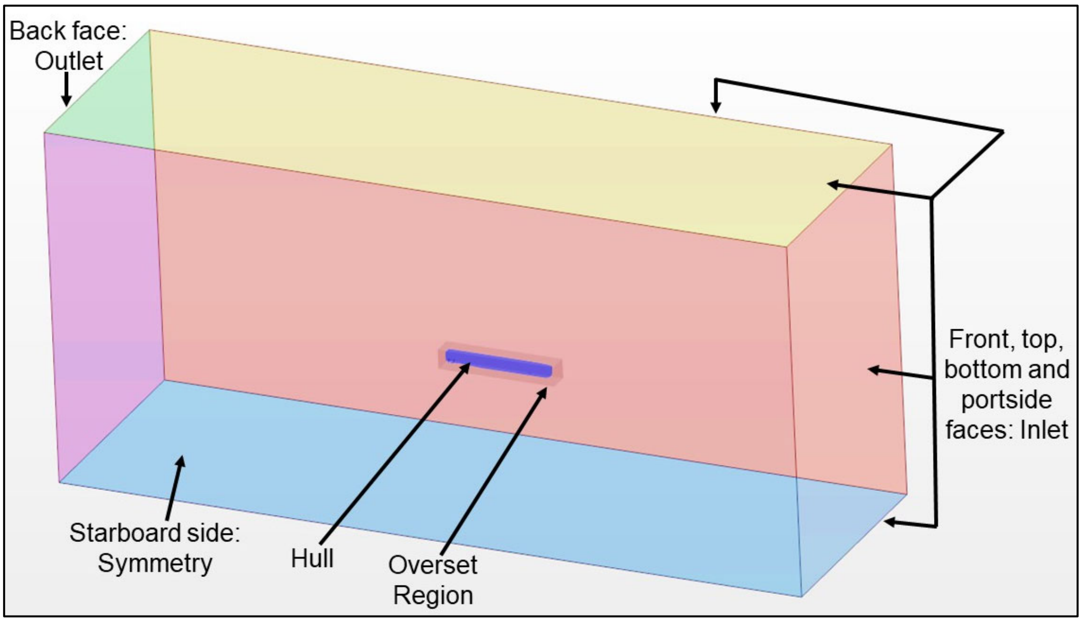

Figure 3. Boundary conditions in CFD simulations of the catamaran.

The Chimera or overset grid technique can provide high accurate dynamic solutions without any deformation on the grid cells around the moving body on that matter. The flow field is divided into two main regions, background and overset, and the flow information is transferred between the boundaries of the overset region and the background region overlapping cells through the intersecting points [18]. Coloured representations of the grid cells and information about the data transfer between those cells for catamarans in CFD simulations can be found in the literature [19,20].

In multiphase marine hydrodynamic problems, the interaction field should be handled in the first place rather than the far field. The mesh structure in this study is designed to start finer near the no-ship surfaces and to continue with a rate of change to get coarser in the relatively far points. The inner field between the demihulls and the overset boundary sites are discretized with smaller cells to capture the wave interference well and to provide a smooth transfer of the flow data between the background and overset regions (upper picture in Figure 4). The ideal way of discretizing the free water surface is to use very small and equally-sized cells on that horizontal plane. However, this approach will generate a very dense mesh and will be far more than practical and cost-effective due to the need for high computational power. Instead, a Kelvin-wave adopted grid has been applied in this study to capture the free surface deformations. The density of the grid resolution on the appendages and bow thruster tunnel of the Stavanger Demonstrator have been increased (Figure 5).

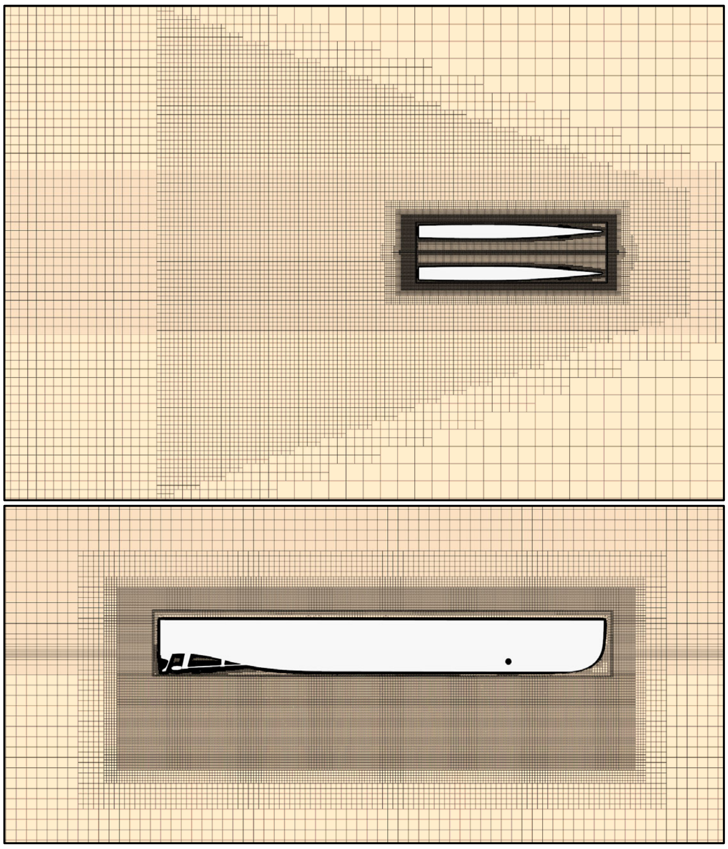

Figure 4. Grid structure on the free water surface (**upper**) and the symmetry plane of a demi-hull (**lower**) in the CFD simulations of the catamaran.

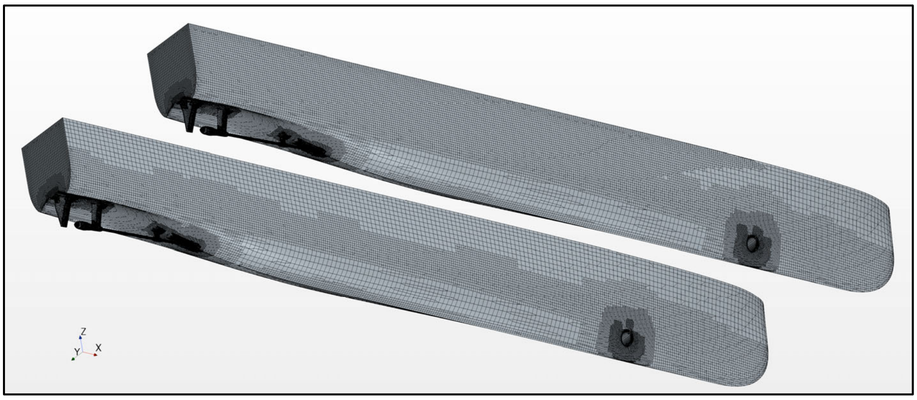

Figure 5. Grid structure on the fully-appended Stavanger Demonstrator.

2.2.3. Form Factor Prediction Method

There are two well-known and widely adopted ways of predicting the form factors of marine vessels: (1) Prohaska's method [21] and (2) the double-body geometric approach or the 1978 ITTC power prediction method [22]. The first method assumes that the wave-making resistance can be represented by the fourth order of the Froude number at low speeds (mostly between 0.10–0.20), and the total resistance coefficient can be written as in Equations (5) and (6). The principle is based on having a linear change at low speeds when the C_T/C_{F0} is plotted against Fr^4/C_{F0} where the intersection point of the linear curve and the C_T/C_{F0} axis gives the form factor (1 + k). Although it is a commonly adopted and well-defined method, Prohaska's method yields reliable results at low speeds.

$$C_T = (1+k)C_{F0} + C_w \tag{5}$$

$$\frac{C_T}{C_{F0}} = (1+k) + a\frac{Fr^4}{C_{F0}} \tag{6}$$

The second method, on the other hand, can even be utilized at high speeds. The methodology is simply cutting the hull form from the free water surface and eliminating the free surface effects by means of reducing the problem to a single-phase fluid dynamics case. The physical practice of this approach is testing the mirrored ship model in an adequate depth of water, like a submarine, and measuring the total resistance of the double-body. In this case, the total resistance is formed of viscous components only (Equation (7)). The form factor (1 + k) can be obtained by dividing the total resistance co-efficient by the frictional resistance coefficient (C_T/C_{F0}). Modelling this numerical problem is relatively less complicated compared to multi-phase simulations.

$$C_T = (1+k)C_{F0} \tag{7}$$

2.3. Presentation of Data

The force units are nondimensionalised by following the Equation (8), where it is necessary. X and Y represent and scalar force units, r is the fluid density, U is the ship advance speed and the S stands for the wetted surface area. The lengths are nondimensionalized by the ship length. All the calculations reported here have been done by using the fully appended catamaran's main particulars, i.e., S includes both hulls' and appendages' wetted surface areas unless the opposite is stated. The C_{F0} frictional resistance coefficient has been calculated by following the ITTC′57 frictional resistance coefficient formula given in Equation (9) [23]. The experimental resistance results have been decomposed by subtracting the C_{F0} from the C_T values that were measured in the experiments (Equation (10)). However, the frictional resistance C_{F0} has been calculated by the wall function that is implemented in the turbulence model in CFD simulations. The corresponding Froude numbers are also calculated using Equation (11) and provided in the tabulated results.

$$X',\ Y' = \frac{X,\quad Y}{0.5\rho U^2 S} \tag{8}$$

$$C_{F0} = \frac{0.075}{(\log(Rn-2))^2} \tag{9}$$

$$C_T = C_{F0} + C_R \tag{10}$$

$$Fr = \frac{U}{\sqrt{gL_{WL}}} \tag{11}$$

3. Results and Discussion

3.1. Verification and Validation Study

The Stavanger Demonstrator hull form was tested in an HSVA experimental towing tank at a wide range of advance speeds [11]. The verification and validation study has been conducted for the LC1 loading condition in deep water due to the available experimental data.

3.1.1. Verification

Even though the comparison between the computational results and the experiments is a strong indication of the reliability of the method used, an uncertainty assessment is essential to draw the limits of the outputs and to observe the convergence of the method from a numerical analysis point of view. Therefore, the latest solution verification techniques, Grid Convergence Index (GCI), Correction Factor (CF) and Factors of Safety (FS) have been applied to calculate the uncertainties in the computations [24–27]. All those three methods are based on Richardson extrapolation. The total grid cell numbers are increased by changing the dimensions of the reference cell by $\sqrt{2}$ as recommended by ITTC [28]. Since the verification procedure is applied to a three-dimensional problem, the ratio between the total grid cell numbers of different qualities is defined as follows (Equation (12)):

$$r_{21} = \left(\frac{N_1}{N_2}\right)^{\frac{1}{3}} r_{32} = \left(\frac{N_2}{N_3}\right)^{\frac{1}{3}} \tag{12}$$

where N_1, N_2, and N_3 are the total cell numbers and $N_3 < N_2 < N_1$. The difference between any numerical scalar result, which, in this case, is the total resistance between two different grid cells, can be calculated as follows (Equation (13)):

$$E_{21} = X_2 - X_1 \; E_{32} = X_3 - X_2 \tag{13}$$

The convergence condition of the numerical solution can then be observed by dividing the constants calculated in Equation (13): $R = E_{21}/E_{32}$. The mathematical meaning of the ratio R is described in Equation (14) and the details can be found in the related reference [29].

$$\begin{gathered} -1 < R < 0 \text{ Oscillatory convergence} \\ 0 < R < 1 \text{ Monotonic convergence} \\ R < -1 \text{ Oscillatory divergence} \\ 1 < R \text{ Monotonic divergence} \end{gathered} \tag{14}$$

Three different grid qualities have been tested at the 0.45 Froude number to calculate the total resistance of the Stavanger Demonstrator at LC1 (Table 3).

Table 3. Resistance values at *Fr* = 0.45 by different grid qualities.

Grid Quality	Total Cell Numbers	C_T (1 × 10^3)
Fine	8.36×10^6	6.345
Medium	4.82×10^6	6.512
Coarse	2.92×10^6	6.648

The total resistance values gradually decrease as the grid resolution becomes dense. Although it seems to have monotonic convergence characteristics, it should be noted that the convergence condition R is the ultimate indication of this behaviour (Table 4). The highest uncertainty is calculated as 10% by the FS method, which is more up-to-date and already known as a conservative method in the literature [12,30].

Table 4. Uncertainty assessment results.

	GCI	CF	FS
r_{21}	1.20	1.20	1.20
r_{32}	1.18	1.18	1.18
R	0.73	0.73	0.73
P_{th}	2.00	2.00	2.00
P_{RE}	2.19	2.19	2.19
$C_{T\text{-}Ext}$ (1×10^3)	6.213	6.213	6.213
SF	1.25	1.12	1.10
Δ (%)	3.90	3.86	10.01

3.1.2. Validation

The validation of the numerical results has been achieved by comparing the resistance components and dynamic behaviour of the Stavanger Demonstrator with the experiments. Since the hull form and the tested conditions are symmetric about the centreline of the catamaran, the rest of the simulations, including double-body analyses have been carried out by adopting the half-body technique to save computational power and time. The experiments of the fully appended catamaran were conducted in HSVA towing tank for the T′ = 0.045 loading condition (LC1) [11].

Validation has been done through the resistance components and the dynamic behaviour of the Stavanger Demonstrator at model scale. The catamaran has been subjected to resistance simulations at a 0.24–0.63 Froude range with all appendages (rudder, shaft, and strut).

A significant match has been reported between the CFD results and those obtained by the experiments. The numerical total resistance values of the catamaran reflect the trend of the experimental results with good accuracy (Figure 6). The maximum relative error between the total resistance values is −3.32% at 0.39 Froude number (Table 5). The negative percentage means that the CFD gives higher values than the corresponding experimental results (see the formulation in Section 2.3). The experimental frictional resistance values have been calculated by using the ITTC′57 formula. The average relative percentage error between $C_{F\text{-}CFD}$ and $C_{F\text{-}Exp}$ has been calculated as approximately 5.6%, which can be concluded with the proven-functionality of the turbulence model (Table 5). The dynamic behaviour of the vessel, especially the extremum locations through the increasing advance speed, has been well-predicted with the CFD method (Figure 7).

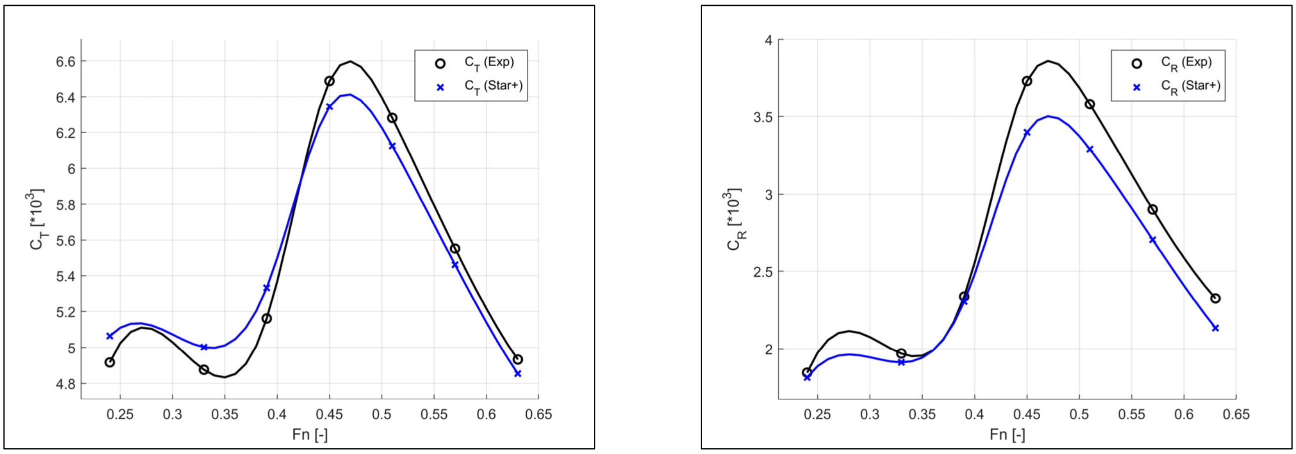

Figure 6. Numerical total (**left**) and residual (**right**) resistance values compared to the experiments.

Table 5. Resistance comparison for LC1.

Fr	$C_{T\text{-}CFD}$ (1 × 10^3)	$C_{T\text{-}Exp}$ (1 × 10^3)	e_{CT} (%)	$C_{F\text{-}CFD}$ (1 × 10^3)	$C_{F\text{-}Exp}$ (1 × 10^3)	e_{CF} (%)
0.24	5.064	4.917	−2.98%	3.248	3.071	−5.75%
0.33	5.002	4.876	−2.59%	3.089	2.906	−6.31%
0.39	5.332	5.161	−3.32%	3.028	2.825	−7.21%
0.45	6.345	6.488	2.21%	2.947	2.758	−6.87%
0.51	6.125	6.281	2.48%	2.837	2.701	−5.01%
0.57	5.461	5.552	1.65%	2.756	2.652	−3.91%
0.63	4.854	4.933	1.60%	2.720	2.610	−4.24%

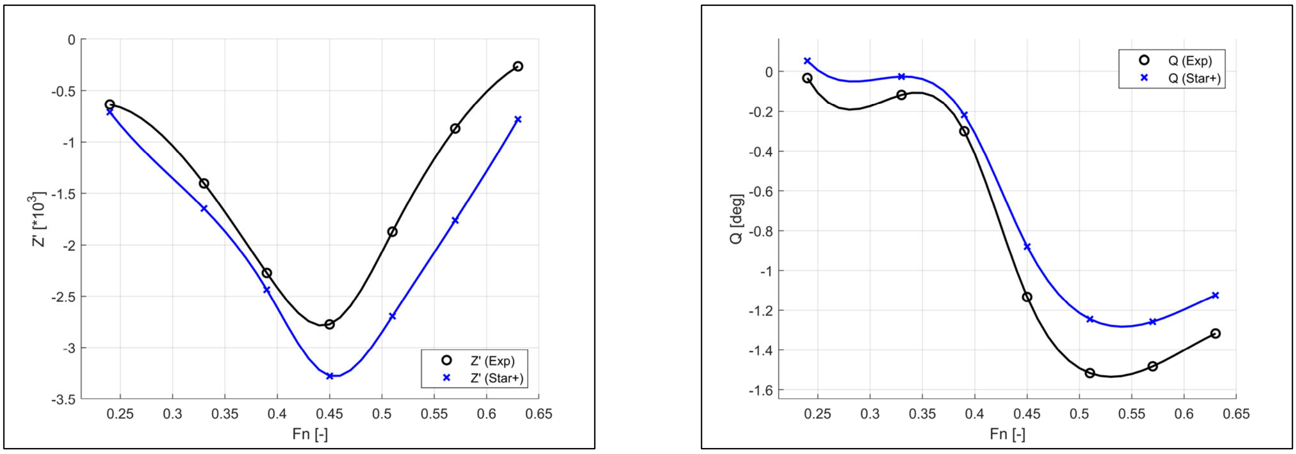

Figure 7. Numerical sinkage (**left**) and trim (**right**) values compared to the experiments.

The relative percentage between the numerical and experimental motion amplitudes are relatively high, yet these values are small enough to cause such high percentages. The difference in motion amplitudes can be the result of measuring points during the experiments, mounting conditions and, of course, the uncertainties in measurement systems and in computational analysis. The numerical uncertainty due to the selected grid system is reported in the previous section, yet no data was provided by the experimental facility regarding uncertainties in measurement systems. It can be noticed that the maximum sinkage values in both methods are obtained between 0.45–0.51 Froude numbers (Table 6). After this point, the catamaran enters the planning regime and the sinkage values decrease gradually (Figure 7).

Table 6. Full scale sinkage and trim comparison for LC1.

Fr	Z'_{CFD} (1 × 10^3)	Q_{CFD} (deg)	Z'_{Exp} (1 × 10^3)	Q_{Exp} (Deg)
0.24	−0.710	0.052	−0.635	−0.033
0.33	−1.649	−0.026	−1.404	−0.117
0.39	−2.436	−0.218	−2.273	−0.300
0.45	−3.276	−0.879	−2.774	−1.133
0.51	−2.694	−1.245	−1.872	−1.517
0.57	−1.763	−1.258	−0.869	−1.483
0.63	−0.779	−1.124	−0.267	−1.317

3.2. Deep and Shallow Water Resistance Analysis Results

The Stavanger Demonstrator has been analysed in deep and shallow water conditions at LC2 to observe the shallow water effects on the resistance and motion characteristics of the vessel. Deep water analyses have been performed in a 1.69 L depth body of water by assigning the bottom of the computational domain as the velocity inlet, which provides an identical numerical set-up to the actual physical conditions (see Section 2.2.2). In a real environment where the fluid is assumed to be still, with no other external effects such as wind and current, the ship travels at a certain speed. To imitate the physical conditions, the ship is captive (free to sink and trim) and the free stream passes through the surface of the vessel in the virtual environment (Figure 8, left caption). Seabed assumptions are extremely important when it comes to having an interaction with the floating body. A ship travelling in a finite depth water will be affected by the presence of the seabed to a certain level. When there is no current or wind, both the current and the seabed will have no speed but relative speed against the advancing vessel, i.e., the current and the seabed will have zero absolute speed. To have an identical numerical solution for the shallow water conditions, the vessel is kept captive (free to sink and trim) and the fluids enter the computational domain on the inlet faces and flow at the operational speed of the vessel; additionally, the seabed boundary condition is set to move in the longitudinal direction at the operational speed of the vessel by having no-slip surface properties (Figure 8, right caption).

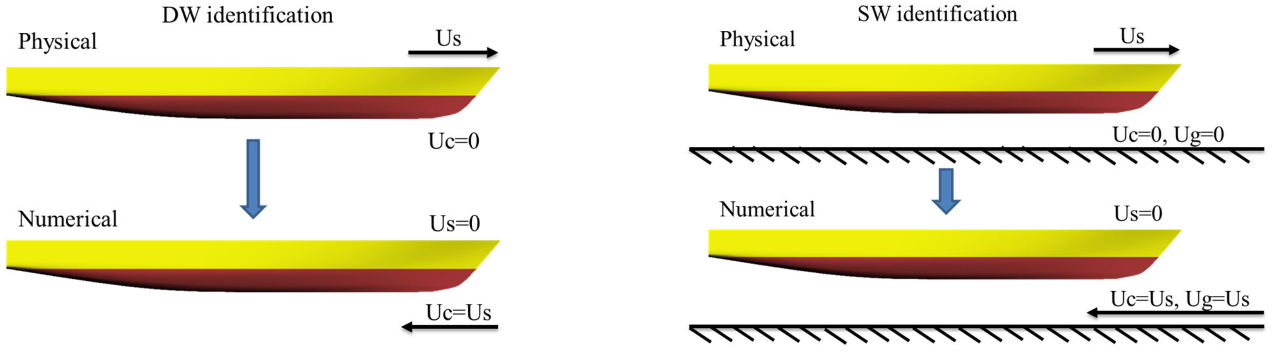

Figure 8. Illustrations for the identical numerical set-up for deep water (**left**) and shallow water (**right**).

The water depth for the shallow water analysis was set to 2.15 m to investigate the Stavanger Demonstrator's dynamic behaviour in potential operational conditions on the Thames River in London. The ratio between the water depth and the draught (H/T) becomes 1.79, which is a strong indication of the interaction between the free surface and the seabed, as practiced in many studies in the literature. The 2-DoF deep water resistance simulations have been performed at all speeds for comparison purpose. Resistance characteristics at LC2 have been reported to be in line with the LC1 validation case. Similarities between the sinkage and trim behaviours can be seen (Figures 7 and 9). The most striking result from the 2-DoF shallow water resistance analyses is the dramatic increase in the residual resistance between the 0.20–0.39 Froude numbers compared to the deep-water results (Figure 10, bottom caption). Interestingly, even though the advance speed increases, the total resistance coefficients remain around 4.6×10^{-3} in shallow water and start to increase after the 0.39 Froude number (Figure 10, top-left caption). The intersection point of two resistance curves has been plotted between 0.39–0.45 Froude numbers at where the shallow water effects turn in favour of the catamaran's resistance performance (Tables 7 and 8). The $Fr = 0.24$ has been identified as the critical speed where the shallow water effects reach the peak point. It should be noted that the highest impact has been detected due to pressure-based resistance components as no noticeable difference has been detected in the frictional resistance component (Figure 10, top-right caption). This was the authors' primary source of motivation in conducting this work to investigate the pressure-based resistance components by carrying on one step further and utilizing the double-body approach to investigate the wave-making resistance component.

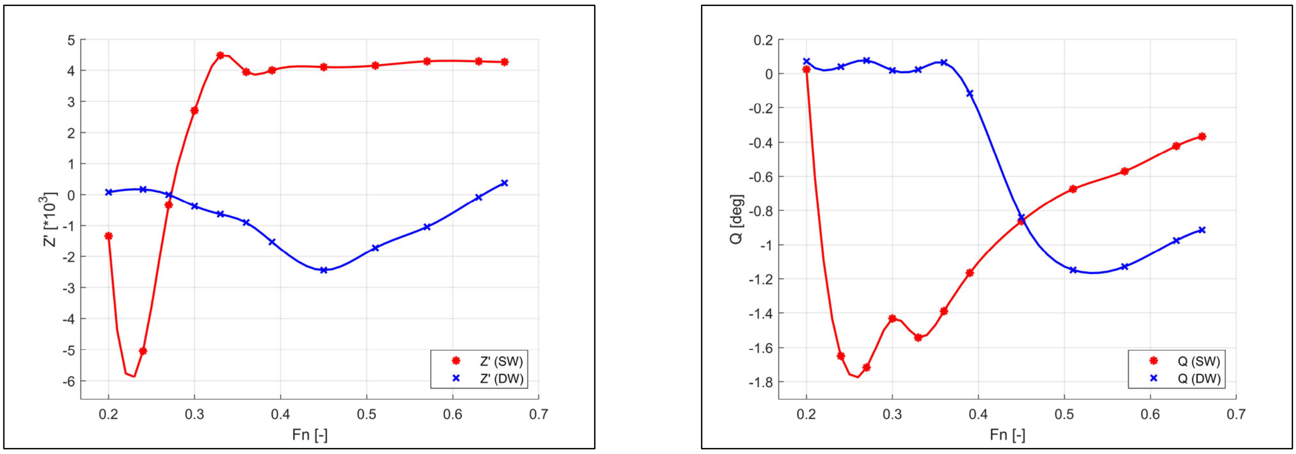

Figure 9. Sinkage (**left**) and trim (**right**) results of the catamaran in deep and shallow water.

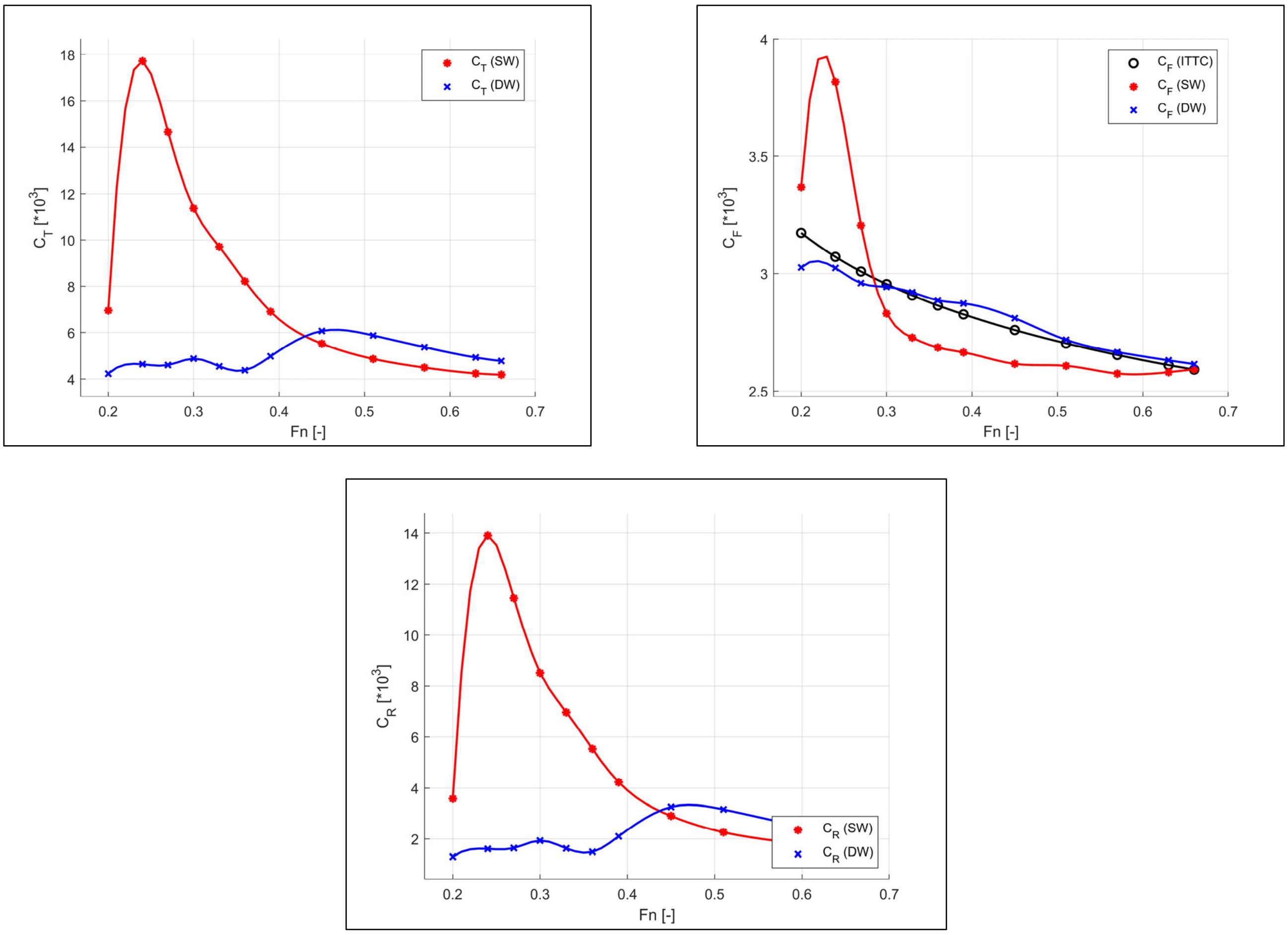

Figure 10. Total (**top-left**), frictional (**top-right**), and residual (**bottom**) resistance results of the catamaran in deep and shallow water at LC2.

Table 7. Resistance results of the catamaran in deep and shallow water at LC2.

Fn	$C_{T\text{-}DW}$ (1 × 10^3)	$C_{F\text{-}DW}$ (1 × 10^3)	$C_{T\text{-}SW}$ (1 × 10^3)	$C_{F\text{-}SW}$ (1 × 10^3)	e_{CT} (%)	e_{CF} (%)
0.20	4.233	3.026	6.952	3.369	−64.2%	−11.3%
0.24	4.634	3.024	17.720	3.817	−282.4	−26.2
0.27	4.601	2.959	14.657	3.206	−218.6	−8.3
0.30	4.875	2.943	11.362	2.830	−133.1	3.8
0.33	4.545	2.920	9.707	2.726	−113.6	6.6
0.36	4.377	2.886	8.212	2.684	−87.6	7.0
0.39	4.973	2.873	6.900	2.664	−38.8	7.3
0.45	6.066	2.810	5.515	2.615	9.1	7.0
0.51	5.872	2.717	4.864	2.607	17.2	4.1
0.57	5.368	2.665	4.492	2.574	16.3	3.4
0.63	4.924	2.630	4.244	2.580	13.8	1.9
0.66	4.773	2.614	4.189	2.592	12.2	0.8

Table 8. Sinkage and trim values of the catamaran in deep and shallow water.

Fn	Z'_{DW} (1 × 10^3)	Z'_{SW} (1 × 10^3)	Q_{DW} (Deg)	Q_{SW} (Deg)
0.20	0.0788	−1.3383	0.0709	0.0235
0.24	0.1690	−5.0447	0.0390	−1.6505
0.27	−0.0017	−0.3331	0.0759	−1.7179
0.30	−0.3753	2.6961	0.0177	−1.4326
0.33	−0.6346	4.4842	0.0222	−1.5421
0.36	−0.9065	3.9456	0.0637	−1.3896
0.39	−1.5303	4.0002	−0.1157	−1.1658
0.45	−2.4447	4.1026	−0.8402	−0.8632
0.51	−1.7202	4.1489	−1.1490	−0.6744
0.57	−1.0439	4.2890	−1.1295	−0.5704
0.63	−0.0822	4.2859	−0.9756	−0.4221
0.66	0.3753	4.2635	−0.9136	−0.3666

The CFD results have been further examined via visual media. The shock wave has been detected in the fore part of the catamaran at the 0.24 Froude number (Figure 11) and at other speeds up to the 0.45 Froude number. The wave contours have been formed more linear than deep water. The extremum points of the wave crest and wave trough ((ζ/L)E3) at model scale have been noted as 9.37 and −11.24 in deep water while 28.12 and −16.87 in shallow water, respectively. The phase distributions on the demihull at Fr = 0.24 shows that the numerical ventilation has not occurred in CFD simulations (Figure 12: blue represents the air phase on the catamaran hull and the water anywhere else). Squat effects in shallow water are strongly related to the velocity field beneath the hull. In the aft region, a noticeable increase in flow velocity has been observed (Figure 13). The decrease in flow speed in the fore region can be considered as a potential cause of the shock wave incidence.

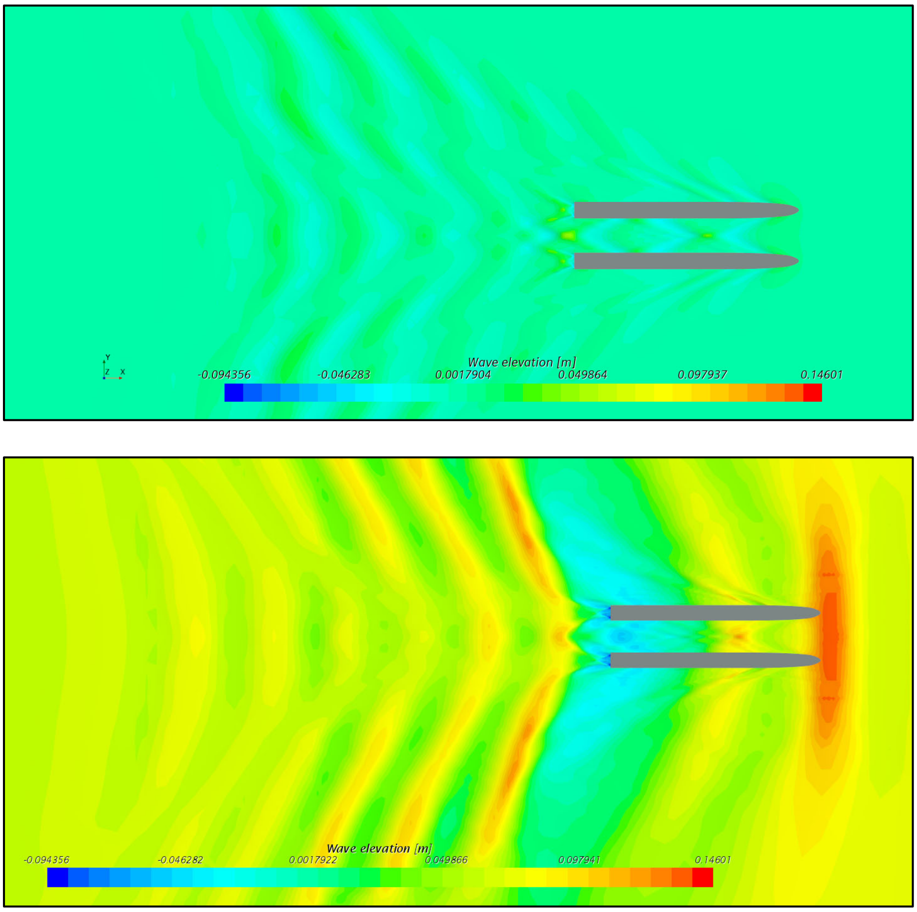

Figure 11. Free surface waves at Fr = 0.24 in deep (**top**) and shallow (**bottom**) water.

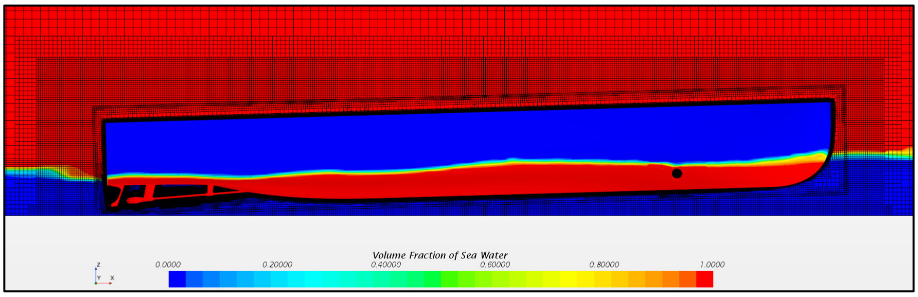

Figure 12. Phase distributions at Fr = 0.24 in shallow water.

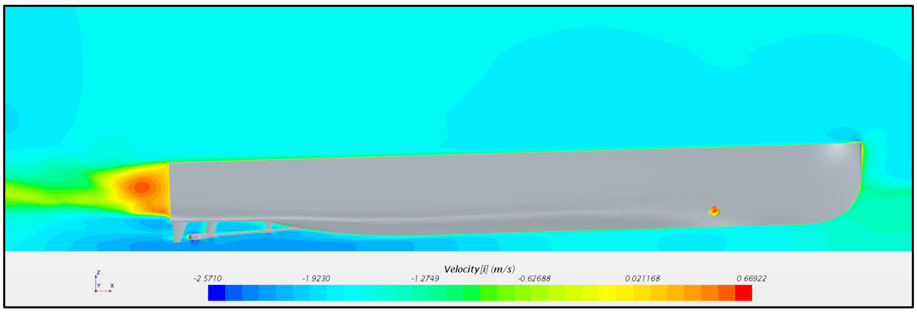

Figure 13. Velocity contours on the centre plane of the demihull at Fr = 0.24 in shallow water.

3.3. Double-Body Analysis Results

The form factors of the catamaran have been predicted by utilizing the double-body approach in CFD simulations. The hull form has been cut from the free surface level and subjected to a series of single-phase CFD simulations at all speeds in both deep and shallow water conditions. The form factors obtained in shallow water were found to be higher than those calculated in deep water for all speeds (Figure 14). The non-linear behaviour of the form factor values in deep water can be correlated by the steep change of the residual resistance component in 2-DoF simulations between 0.39–0.57 Froude numbers (see Figure 10, bottom caption). No matter which operational condition is chosen, form factors tend to have higher values with increasing speeds, which is in accordance with the literature findings. The maximum form factor has been calculated as 1.41 and 1.39 for the shallow and deep-water conditions at maximum speed, respectively.

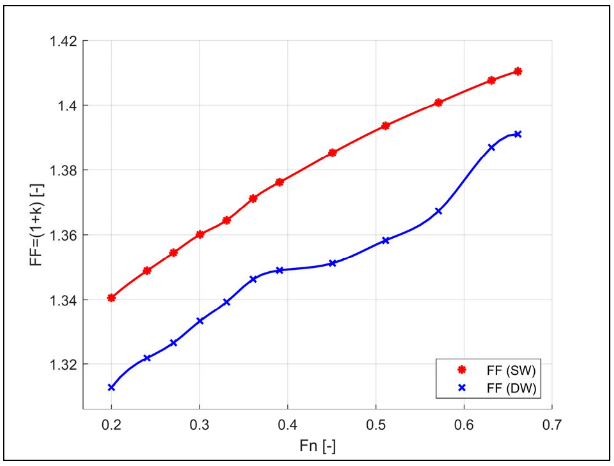

Figure 14. Form factors in deep and shallow water conditions.

The velocity distributions on the centre plane of the demihull at Fr −0.24 are presented in Figure 15 for the deep and shallow waters. Here, the submerged part of the catamaran is mirrored to obtain the double-body form, which has a similar 3-D shape to submarines. It can be noticed that the flow speed is higher when the fluid particles pass through the mid-body in the shallow water case (Figure 15, bottom caption).

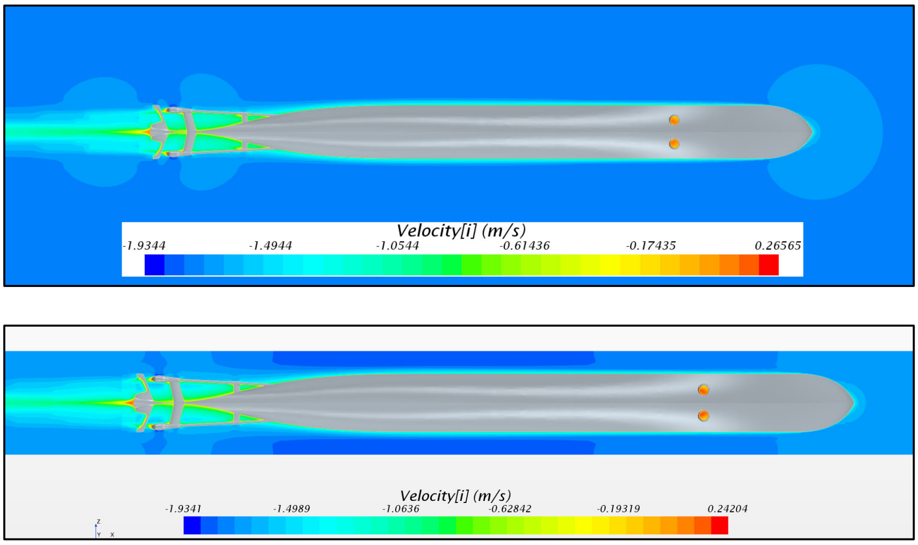

Figure 15. Velocity contours on the centre plane of the demihull at Fr = 0.24 in deep (**top**) and shallow (**bottom**) waters.

3.4. Wave-Making Resistance Calculations

The 2-DoF CFD simulations have provided the frictional (C_F) and residual resistance (C_R) components of the catamaran in deep and shallow waters. The output of the double-body analyses, form factors, have been used to decompose the pressure-based resistance into viscous pressure (C_{VP}) and gravitational waves (C_W) by following the 1978 ITTC power prediction method. The wave-making resistance coefficients are presented in Figure 16 and tabulated in Table 9. Nondimensional analysis of the wave-making resistance shows that the interaction between the hull and seabed becomes extremely important, even at moderate and relatively low speeds. The two peak points at Fr = 0.30 and Fr = 0.45 in deep water is no longer observed in shallow water results. Instead, gradually decreasing wave-making resistance values can be noticed with increasing speeds. Under the conditions defined in this study, it can be concluded that the shallow water effects are significantly dominant between 0.24–0.39. After passing the transition Froude number, which has been reported to be between 0.39–0.45, shallow water effects start to work in favour of the resistance performance of the catamaran.

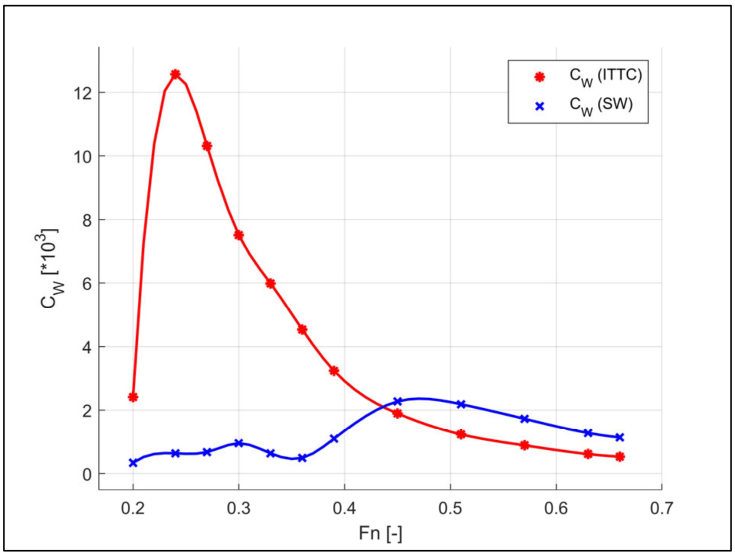

Figure 16. Wave-making resistance coefficients of the catamaran.

Table 9. Wave-making resistance values at LC2.

Fn	***FF$_{SW}$***	***C$_{W\text{-}SW}$***	***FF$_{DW}$***	***C$_{W\text{-}DW}$***
0.20	1.3406	2.41×10^3	1.3128	3.40×10^4
0.24	1.3489	1.26×10^2	1.3219	6.36×10^4
0.27	1.3545	1.03×10^2	1.3266	6.75×10^4
0.30	1.3601	7.51×10^3	1.3334	9.51×10^4
0.33	1.3644	5.99×10^3	1.3393	6.35×10^4
0.36	1.3712	4.53×10^3	1.3463	4.92×10^4
0.39	1.3762	3.23×10^3	1.3490	1.10×10^3
0.45	1.3853	1.89×10^3	1.3512	2.27×10^3
0.51	1.3936	1.23×10^3	1.3583	2.18×10^3
0.57	1.4008	8.86×10^4	1.3673	1.72×10^3
0.63	1.4076	6.12×10^4	1.3870	1.28×10^3
0.66	1.4104	5.33×10^4	1.3910	1.14×10^3

4. Conclusions

This study was conducted to look for insight into the resistance components, especially the wave-making resistance of a zero-emission fast catamaran ferry. The subject vessel, the Stavanger Demonstrator catamaran, was built and named MS Medstraum in Norway as a demonstrator of an ongoing H2020 project TrAM.

The catamaran has been analysed under free surface effects in deep and shallow water conditions to obtain resistance values and to observe the dynamic behaviour of the vessel. The 2-DoF CFD simulation results show a significantly good match with the experiments. It has been noted that the highest impact of the shallow water effects is on the residuary resistance component as no noticeable difference has been detected in the frictional resistance. The transition speed where the shallow water effects start to work in favour of the resistance performance of the catamaran has been recorded between the 0.39–0.45 Froude numbers. The critical speed, where the total resistance reaches the maximum point due to shallow water effects, has been recorded at $Fr = 0.24$. The catamaran travels at negligible trim angles up to $Fr = 0.39$; however, from this point on, the trim values increase exponentially towards the aft. On the other hand, significant trim-to-aft conditions occur in shallow water. The vertical motion of the catamaran is completely in the opposite direction in deep and shallow waters. Shock waves in the fore part of the catamaran have been captured at moderate and relatively small advance speeds in shallow water.

The study is followed by utilizing the double-body approach at all speeds in both deep and shallow water conditions. The form factors of the catamaran have been calculated for each speed and used to decompose the residual resistance (C_R) components into viscous pressure (C_{VP}) and wave-making resistance (C_W). Regardless of the operational condition, the form factors have been found to have higher values with increasing speeds, which complies with the literature. The analysis of the wave-making resistance shows that the interaction between the hull and seabed becomes extremely important even at moderate and relatively low speeds. In fact, the total resistance values of shallow water cases become lower than those obtained in deep water because of the significant reduction in wave-making resistance due to the interaction between the gravitational waves and the riverbed. This statement is not valid for low Froude numbers as the resistance of the catamaran increases dramatically at lower speeds.

The hydrodynamic performance of the Stavanger Demonstrator will be further investigated for changing depth, different loading conditions, and demihull clearance. The propeller effects will be taken into consideration in future studies.

Author Contributions: Conceptualization, S.D. and E.B.; methodology, S.D.; software, S.D. and M.Z.A.; validation, S.D., M.Z.A., X.X. and A.N.; formal analysis, M.Z.A. and X.X.; investigation, M.Z.A. and A.N.; resources, X.X.; data curation, A.N.; writing—original draft preparation, S.D.; writing—review and editing, E.B.; visualization, S.D. and A.N.; supervision, E.B.; project administration, E.B.; funding acquisition, E.B. All authors have read and agreed to the published version of the manuscript.

Funding: This work was funded by the H2020 European Union project "TrAM—Transport: Advanced and Modular" under the contract number 769303.

Institutional Review Board Statement: Not applicable.

Informed Consent Statement: Not applicable.

Data Availability Statement: Not applicable.

Acknowledgments: The authors affiliated with MSRC greatly acknowledge the funding from DNV and Royal Caribbean Group for the MSRC's establishment and operation. The opinions expressed herein are those of the authors and do not reflect the views of DNV and Royal Caribbean Group. CFD simulations run by the University of Strathclyde were performed on the ARCHIE-WeSt High Performance Computer (www.archie-west.ac.uk (accessed on 8 November 2022)).

Conflicts of Interest: The authors declare no conflict of interest.

Nomenclature

α	Constant
B, B_M	Beam moulded (m)
C_F, C_{F0}	Frictional drag coefficient
C_T	Total drag coefficient
$C_{T\text{-}CFD}$	Total drag coefficient by CFD
$C_{T\text{-}Exp}$	Total drag coefficient by experiments
$C_{T\text{-}Ext}$	Extrapolated total drag coefficient
ε	Relative Error (%)
λ	Model scale ratio
L, L_{PP}	Length between perpendiculars (m)
L_{WL}	Length of waterline (m)
v	Kinematic viscosity (N s m^{-2})
∇	Displacement volume (m^3)
r	Density of water (kg m^{-3})
P	Pressure (N m^{-2})
Q	Pitch Amplitude (deg)
R	Convergence Condition
S	Wetted hull surface area (m^2)
T	Draught at Midship (m)
u, v, w	Fluid velocity components
$y+$	Dimensionless wall distance
Z	Heave Amplitude (m)
ζ	Wave height (m)
$(1 + k)$	Form Factor
BCs	Boundary Conditions
CF	Correction Factor
CFD	Computational Fluid Dynamics
DC372	Delft Catamaran 372
DoF	Degree of Freedom
EFD	Experimental Fluid Dynamics
Fr, Fn	Froude Number
FS	Factors of Safety
GCI	Grid Convergence Index
H2020	Horizon 2020
HSVA	Hamburg Ship Model Basin
ITTC	International Towing Tank Conference
KB	Vertical Centre of Buoyancy
LC	Loading Condition
LCB	Longitudinal Centre of Buoyancy
RANS	Reynolds-averaged Navier–Stokes
TrAM	Transport: Advanced and Modular
WAM-V	Wave adaptive modular vessel
VoF	Volume of Fluid

References

1. Molland, A.; Wellicome, J.; Couser, P. *Resistance Experiments on a Systematic Series of High Speed Displacement Catamaran Forms: Variation of Length-Displacement Ratio and Breadth-Draught Ratio*; Ship Science Report No. 71; University of Southampton: Iskandar Puteri, Malaysia, 1994.
2. Insel, M.; Doctors, L.J. Wave pattern prediction of monohulls and catamarans in a shallow-water canal by linearised theory. In Proceedings of the 12th Australian Fluid Mechanics Conference, Sydney, NSW, Australia, December 1995; pp. 259–262. Available online: https://www.afms.org.au/proceedings/12/Insel_and_Doctors_1995.pdf (accessed on 22 November 2022).
3. Veer, R.V. *Experimental Results of Motions, Hydrodynamic Coefficients and Wave Loads on the 372 Catamaran Model*; Technical Report 1129; Delft University of Technology: Delft, The Netherlands, 1998.

4. Castiglione, T.; He, W.; Stern, F.; Bova, S. Effects of shallow water on catamaran interference. In Proceedings of the 11th International Conference on FAST2011, Honolulu, HI, USA; 26–29 September 2011.
5. Milanov, E.; Chotukova, V.; Stern, F. System Based Simulation of Delft372 Catamaran Maneuvering Characteristics as Function of Water Depth and Approach Speed. In Proceedings of the 29th Symposium on Naval Hydrodynamics, Gothenburg, Sweden, 26–31 August 2012.
6. Broglia, R.; Jacob, B.; Zaghi, S.; Stern, F.; Olivieri, A. Experimental investigation of interference effects for high-speed catamarans. *Ocean. Eng.* **2014**, *76*, 75–85. [CrossRef]
7. Begovic, E. Wave Interference Prediction of a Trimaran Using Form Factor. In *HSMV 2020: Proceedings of the 12th Symposium on High Speed Marine Vehicles*; IOS Press: Amsterdam, The Netherlands; Volume 5, p. 99.
8. Bašić, J.; Blagojević, B.; Andrun, M. Improved estimation of ship wave-making resistance. *Ocean. Eng.* **2020**, *200*, 107079. [CrossRef]
9. Papanikolaou, A.; Xing-Kaeding, Y.; Strobel, J.; Kanellopoulou, A.; Zaraphonitis, G.; Tolo, E. Numerical and Experimental Optimization Study on a Fast, Zero Emission Catamaran. *JMSE* **2020**, *8*, 657. [CrossRef]
10. Boulougouris, E.; Papanikolaou, A.; Dahle, M.; Tolo, E.; Xing-Kaeding, Y.; Jürgenhake, C.; Seidenberg, T.; Sachs, C.; Brown, C.; Jenset, F. Implementation of Zero Emission Fast Shortsea Shipping. In Proceedings of the SNAME Maritime Convention; Online, 27–29 October 2021.
11. Shi, G. Numerical investigation of the resistance of a zero-emission full-scale fast catamaran in shallow water. *J. Mar. Sci. Eng.* **2021**, *9*, 563. [CrossRef]
12. Duman, S.; Bal, S. Turn and zigzag manoeuvres of Delft catamaran 372 using CFD-based system simulation method. *Ocean. Eng.* **2022**, *264*, 112265. [CrossRef]
13. Ulgen, K.; Dhanak, M.R. Hydrodynamic Performance of a Catamaran in Shallow Waters. *J. Mar. Sci. Eng.* **2022**, *10*, 1169. [CrossRef]
14. TrAM. Transport: Advanced and Modular (TrAM) Horizon2020 Project. 2022. Available online: https://tramproject.eu/ (accessed on 22 November 2022).
15. Simcenter STAR-CCM+. 2022. Available online: https://www.plm.automation.siemens.com/global/en/products/simcenter/STAR-CCM.html (accessed on 22 November 2022).
16. Hirt, C.W.; Nichols, B.D. Volume of fluid (VOF) method for the dynamics of free boundaries. *J. Comput. Phys.* **1981**, *39*, 201–225. [CrossRef]
17. ITTC. Practical Guidelines for Ship CFD Applications. In Proceedings of the 26th ITTC, Rio de Janerio, Brazil. 2011. Available online: https://ittc.info/media/1357/75-03-02-03.pdf (accessed on 22 November 2022).
18. Benek, J.A.; Steger, J.L.; Dougherty, F.C.; Buning, P.G. Chimera: A Grid-Embedding Technique. AEDC-TR-85-64; Arnold Engineering Development Center: Fort Belvoir, VA, USA, 1986.
19. Begovic, E. Pure Yaw Simulations of Fast Delft Catamaran 372 in Deep Water. In *HSMV 2020: Proceedings of the 12th Symposium on High Speed Marine Vehicles*; IOS Press: Amsterdam, The Netherlands; Volume 5, p. 109.
20. Duman, S.; Bal, S. Prediction of maneuvering coefficients of Delft catamaran 372 hull form. In *Sustainable Development and Innovations in Marine Technologies*, 1st ed.; Georgiev, P., Soares, C.G., Eds.; CRC Press: Boca Raton, FL, USA, 2019; pp. 167–174. [CrossRef]
21. Prohaska, C. A simple method for the evaluation of the form factor and the low speed wave resistance. In *Hydro-and Aerodynamics Laboratory, Lyngby, Denmark, Hydrodynamics Section, Proceedings of the 11th International Towing Tank Conference, ITTC'66*; Resistance Committee: Tokyo, Japan, 1966; pp. 65–66.
22. Hughes, G. Friction and form resistance in turbulent flow, and a proposed formulation for use in model and ship correlation. In National Physical Laboratory, NPL, Ship Division, Presented at the Institution of Naval Architects, Paper no. 7, RINA Transactions, London; April 1954. Available online: https://repository.tudelft.nl/islandora/object/uuid%3A9a642c53-27f0-45fe-a5e4-5e1296b62af1 (accessed on 22 November 2022).
23. ITTC. Report of 8th ITTC Resistance Committee. In Proceedings of the 8th International Towing Tank Conference, Madrid, Spain, September 1957. Available online: https://repository.tudelft.nl/islandora/object/uuid%3A4aa44007-881c-441c-82dd-70f45cc70ff2 (accessed on 22 November 2022).
24. Roache, P.J. Perspective: A Method for Uniform Reporting of Grid Refinement Studies. *J. Fluids Eng.* **1994**, *116*, 405. [CrossRef]
25. Stern, F.; Wilson, R.V.; Coleman, H.W.; Paterson, E.G. Comprehensive Approach to Verification and Validation of CFD Simulations—Part 1: Methodology and Procedures. *J. Fluids Eng.* **2001**, *123*, 793. [CrossRef]
26. Celik, I.B.; Ghia, U.; Roache, P.J.; Freitas, C.J. Procedure for Estimation and Reporting of Uncertainty Due to Discretization in CFD Applications. *J. Fluids Eng.* **2008**, *130*, 078001. [CrossRef]
27. Xing, T.; Stern, F. Factors of Safety for Richardson Extrapolation. *J. Fluids Eng.* **2010**, *132*, 061403. [CrossRef]
28. ITTC. Resistance, Uncertainty Analysis, Example for Resistance Test. In Proceedings of the International Towing Tank Conference. 2002. Available online: https://ittc.info/media/1818/75-02-02-02.pdf (accessed on 22 November 2022).

29. Phillips, T.S.; Roy, C.J. Richardson Extrapolation-Based Discretization Uncertainty Estimation for Computational Fluid Dynamics. *J. Fluids Eng.* **2014**, *136*, 121401. [CrossRef]
30. Korkmaz, K.B. CFD based form factor determination method. *Ocean. Eng.* **2021**, *220*, 108451. [CrossRef]